Numerical simulations of turbulent flow within and in the wake of a small basin

Marwan Katurji,[1,2] Shiyuan Zhong,[1] Michael Kiefer,[1] and Peyman Zawar-Reza[2]

[1]   Small terrain features, such as small valleys, basins, sinkholes, low hills, and outcrops, while generally associated with mountainous regions, can also be found over plains. In this study, we present a numerical investigation of the effect of a small terrain feature (a 30 m high rim) on the mean and turbulent flows inside and downstream of an enclosed basin it surrounds. Results from high-resolution numerical simulations (10 m isotropic spatial resolution) indicate that small terrain features in the proximity of larger ones can induce relatively large modifications to the mean and turbulent flows. The 30 m high rim is found to have an effect on the mean wind speeds at least 600 m upstream from the basin. The main effect is a 10% reduction in wind speed up to 120 m above ground level due to the upstream blocking effect of the rim. The presence of the rim can also double the turbulent kinetic energy (TKE) both inside and downstream of the basin compared to an otherwise identical basin without a rim. The slopes of the basin play an important role in first creating and then defining the wake, and in intermittent wind regimes most of the scalar transport from near the slope of the basin happens through slope roll vortices that define the edge of the downstream wake region of the basin. Inside the basin, the rim acts to limit momentum transfer in the lower half of the basin, which suggests a mechanical forcing effect induced by the rim on lower basin environments that could interact with thermal buoyancy effects in heated or cooled basins. Some of the wake features resemble wind-eroded surfaces in the wakes of Martian craters. Results also reveal a critical height level (43 m below the rim height) that acts as the most favored location for TKE production and destruction, which could be important for the top-to-bottom turbulence erosion of basin boundary layers. These results stress the importance of resolving small-scale terrain features, as their effects can be nonlocal.

1. Introduction

[2] Small terrain features, such as small valleys, basins, sinkholes, low hills, and outcrops, can be found across plains as well as in complex mountainous terrain; these small terrain features may perturb the ambient flow field. Previous studies have investigated terrain-induced turbulence and its feedback on boundary layer atmospheric processes. These investigations had applications with spatial scales from a few hundred meters to a few kilometers. The Mesoscale Alpine Program, carried out in the Rivera Valley, Switzerland [*Bougeault et al.*, 2001; *Volkert and Gutermann*, 2007] highlighted the importance of the spatial variability of turbulent variables in complex terrain [*Rotach and Zardi*, 2007] and

the need to understand the dynamic feedback in relation to flat-terrain boundary layer theory that assumes spatial homogeneity. *Moraes et al.* [2005] showed that flat-terrain similarity theories can extend to complex terrain situations only when the flow retains a memory of upstream flat-terrain conditions before interacting with the complex topography. Interest in terrain-induced turbulence was also extended to aviation safety and prediction of terrain rotors in valley systems and their interaction with mountain wave activity within the Terrain-Induced Rotor Experiment framework [*Doyle et al.*, 2009]. *Katurji et al.* [2011a] reported the flow modifications due to upstream terrain such as steep slopes on observed eddy length scales and alteration of the measured turbulence spectrum the slopes induce for applications like wind turbine siting. Topographic leeside wakes on the planetary boundary layer scale have also been studied and related to topographically triggered precipitation from the basic theory [*Schär and Smith*, 1993; *Smith et al.*, 1997] to large-eddy simulations (LESs) [*Kirshbaum and Smith*, 2009]. The above mentioned studies convey the scientific interest and motivation in studying terrain-induced disturbances in the lower atmosphere and highlight the effect of terrain on downstream ambient conditions for various applications.

---
[1]Department of Geography, Michigan State University, East Lansing, Michigan, USA.
[2]Department of Geography, University of Canterbury, Christchurch, New Zealand.

Corresponding author: M. Katurji, Department of Geography, University of Canterbury, Private Bag 4800, Christchurch, New Zealand. (katurji@msu.edu; marwan.katurji@canterbury.ac.nz)

[3] Small basins or valleys (not necessary inhabited ones) have been attractive to scientists interested in terrain-induced processes and their interactions with the ambient atmosphere because the small size makes it practically and economically feasible to cover the terrain with instruments, allowing one to better capture local circulations and boundary layer structure. When isolated from other complex terrain features, these small basins/valleys can enable focused analyses that provide insight into physical mechanisms governing a specific terrain-related phenomenon. The Meteor Crater Experiment (METCRAX) [*Whiteman et al.*, 2008], carried out in Arizona's Meteor Crater, made use of an isolated small basin to understand various stable boundary layer phenomena such as drainage flows, cold air pooling, gravity waves, and seiches [*Savage et al.*, 2008; *Fritts et al.*, 2010; *Kiefer and Zhong*, 2011; *Whiteman et al.*, 2010; *Lehner and Whiteman*, 2012]. Most of the work conducted as part of METCRAX has focused on mean flows, with the exception of a study by *Fu et al.* [2010] that compared turbulence measured inside the crater with turbulence outside the crater over a flat plain. Their results showed an increase in the crater's surface turbulent kinetic energy (*TKE*) of almost a factor of three relative to the upstream measurement when wind speeds were greater than $5 \, \mathrm{ms}^{-1}$. Although the authors attribute this increase in turbulence to the crater's rim that shelters the crater interior from high wind speed, and thus promotes the transfer of mean kinetic energy to TKE inside the basin, the effect of the rim was not conclusive because of the limitations of the observational field work. The effect of the rim was investigated by *Kiefer and Zhong* [2011] in a two-dimensional numerical modeling study that focused on the temperature structure inside the crater under stable stratification. The authors concluded that the rim has little impact on the development of the temperature structure within the basin. However, their results were from 2D simulations, so the rim's blocking effect and full 3D turbulence structure were not resolved.

[4] The current study was motivated by observational analyses presented in *Fu et al.* [2010] that showed large differences in the turbulence measured inside and outside the small basin. Using fine-scale idealized numerical simulations, we examine the effects of a small basin, similar in size to the Meteor Crater, on both mean flow and turbulence in the surrounding atmosphere. The small size of the basin (on the order of a few hundred meters) makes it ideal to carry out high-resolution turbulence-resolving simulations, using the LES technique, to highlight special features of the flow dynamics. The results will reveal the mean and turbulent flow structure inside and in the wake of the basin under high wind speed conditions $(10 \, \mathrm{ms}^{-1})$ and a neutrally buoyant atmosphere, with specific focus on small terrain features (~30 m high) such as the crater rim and their effects on the momentum and turbulent energy budgets inside and in the wake of the crater.

[5] The results from the three-dimensional simulations presented here may have implications for both terrestrial and extraterrestrial applications. Regarding terrestrial applications, this research can provide guidance on instrument placements around similar topography, assist in observational data analysis, and verify the performance of a mesoscale model at microscale resolution, all of which have implications for wind turbine siting and/or air pollution dispersion in areas with small terrain features. Regarding extraterrestrial applications, this research may have implications

for aeolian features and wind patterns by assisting in the interpretation of observed crater wakes on Mars as outlined in the observational and atmospheric modeling study of Mars's craters [*Greeley et al.*, 2008, 2003].

2. Methodology

[6] The Advanced Regional Prediction System (ARPS) was used to carry out the simulations in this study. Developed by the Center for Analysis and Prediction of Storms at the University of Oklahoma [*Xue et al.*, 2001], ARPS is a nonhydrostatic compressible flow solver of the Navier-Stokes equations, using terrain-following coordinates, applied to a land-atmosphere interaction system and used operationally for weather forecasting. ARPS has been validated in numerous studies for real case scenarios in complex terrain [*Chow et al.*, 2006; *Weigel et al.*, 2006] and compared and verified with a variety of other models under different atmospheric stability regimes [*Fedorovich et al.*, 2004; *Beare et al.*, 2006]. The model was also applied successfully at the spatial resolution of the microscale (less than 100 m) to investigate turbulence structures over forested hills [*Dupont et al.*, 2008; *Fesquet et al.*, 2009], cold-air pooling dynamics [*Colette et al.*, 2003; *Kiefer and Zhong*, 2011; *Katurji and Zhong*, 2012] and long-range transport of *TKE* and flow interaction with terrain [*Katurji et al.*, 2011b].

[7] For this study, ARPS is configured in three-dimensional mode with three different terrain configurations (Figure 1). In the first simulation (*control*), the terrain is characterized by a small, circular basin or sinkhole that is approximately 1200 m wide at the top and 130 m deep with a 30 m high rim, which is similar in dimension to Arizona's Meteor Crater [*Whiteman et al.* 2008]. This simulation is also referred to as the *rim* simulation to distinguish it from the other simulations. The size of the domain is approximately three times the crater width along the stream-wise flow direction, one and a half times the crater width in the crosswind direction, and six times crater depth in the vertical. The second simulation has similar terrain except that the rim on top of the crater is removed and is referred to as the *no-rim* simulation. Finally, the third simulation replaces the crater terrain by flat terrain and is referred to as the *flat* simulation. An isotropic grid resolution of 10 m is used for all three simulations. All simulations are initialized with a horizontally homogeneous atmosphere with constant wind speed of $10 \, \mathrm{ms}^{-1}$ from the crater ground level up to the domain top, and neutral stratification. The surface thermodynamic energy calculations are turned off. This experimental design permits the analysis of the dynamic effects of the terrain on the mean flows and turbulence within and downstream of the small basin. The wave-radiation open boundary condition [*Klemp and Durran*, 1983] is applied at the inflow (west) and outflow (east) boundaries, while the north and south boundaries were treated as periodic. The inflow and initial conditions did not include any turbulent perturbations. This experimental design allows for an investigation into the effects of terrain-induced (crater rim and basin) turbulence only. We intend to explore how the underlying terrain could feedback on the overlying atmosphere limited to the described conditions. Despite the idealized conditions, there are some aspects of reality in the presented simulations. One aspect is the short time scale dynamic
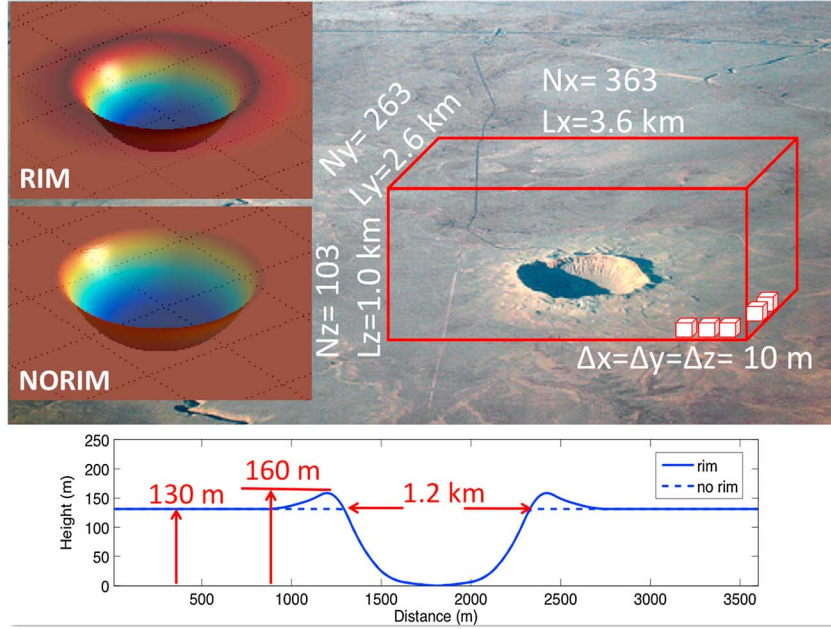
Figure 1. Arizona's Meteor Crater with a layout of modeled topography, domain size, and grid resolution. In addition to the *rim* and *no-rim simulations*, a third simulation, *flat*, was carried out without the crater topography.

response of the boundary layer within and in the wake of a basin to wind gusts and impulsive flow regimes. From this perspective, the simulations could represent a real case where winds accelerate from almost calm conditions to the set wind velocity in the simulations. Another aspect is the steady state evolution of the basin boundary layer under consistently high wind speeds and how the terrain induces feedback in the absence of larger planetary boundary layer turbulence.

[8] The ARPS simulations are conducted in LES mode [*Lilly*, 1967; *Sagaut*, 2001] with a 1.5-order *TKE* subgrid-scale closure scheme. The turbulent momentum diffusion coefficient was calculated from the subgrid-scale *TKE* and length scales that are a function of the grid size for a neutral atmosphere following the *Deardorff* [1980] formulations. To understand the relative contribution of various processes

to the mean and turbulent flows, tendency analysis is performed. For the mean flows, the momentum budget is analyzed. The momentum budget equation in its simplest form can be written as,

$$\frac{\partial \boldsymbol{u}}{\partial t} + A = P + M \qquad (1)$$

where,

$$A = -\boldsymbol{u}.\nabla \boldsymbol{u}$$
$$P = -\frac{1}{\rho}\nabla.p$$
$$M = \nabla.(K.\nabla \boldsymbol{u})$$

where ρ is air density (kgm^{-3}), p is air pressure (Pa), K is eddy viscosity (m^2s^{-1}), and $\boldsymbol{u}$ is mean wind velocity (ms^{-1}). The three dominant terms are the momentum advection (A), the pressure gradient force (P), and the turbulent
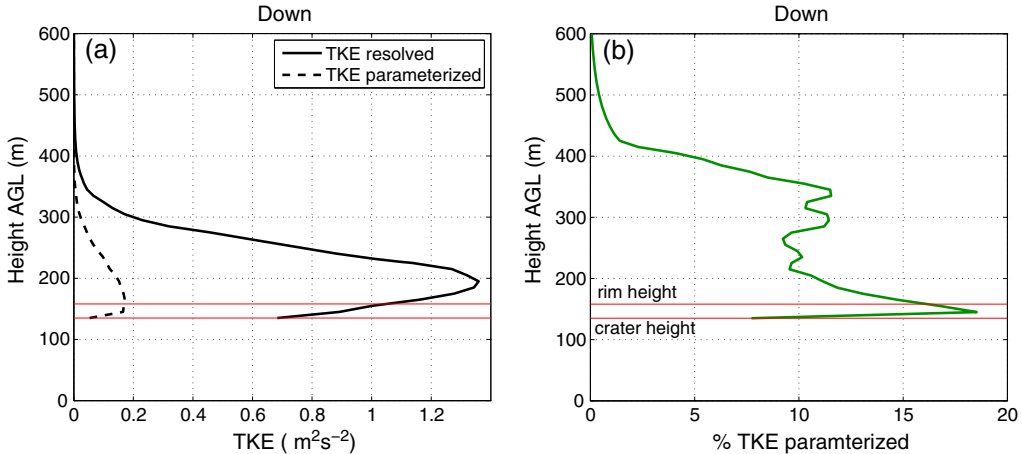

Figure 2. (a) One hour average vertical profile of subgrid scale or parameterized TKE and resolved *TKE* computed from the crater downstream region. (b) Vertical profile of percent parameterized *TKE*.

3
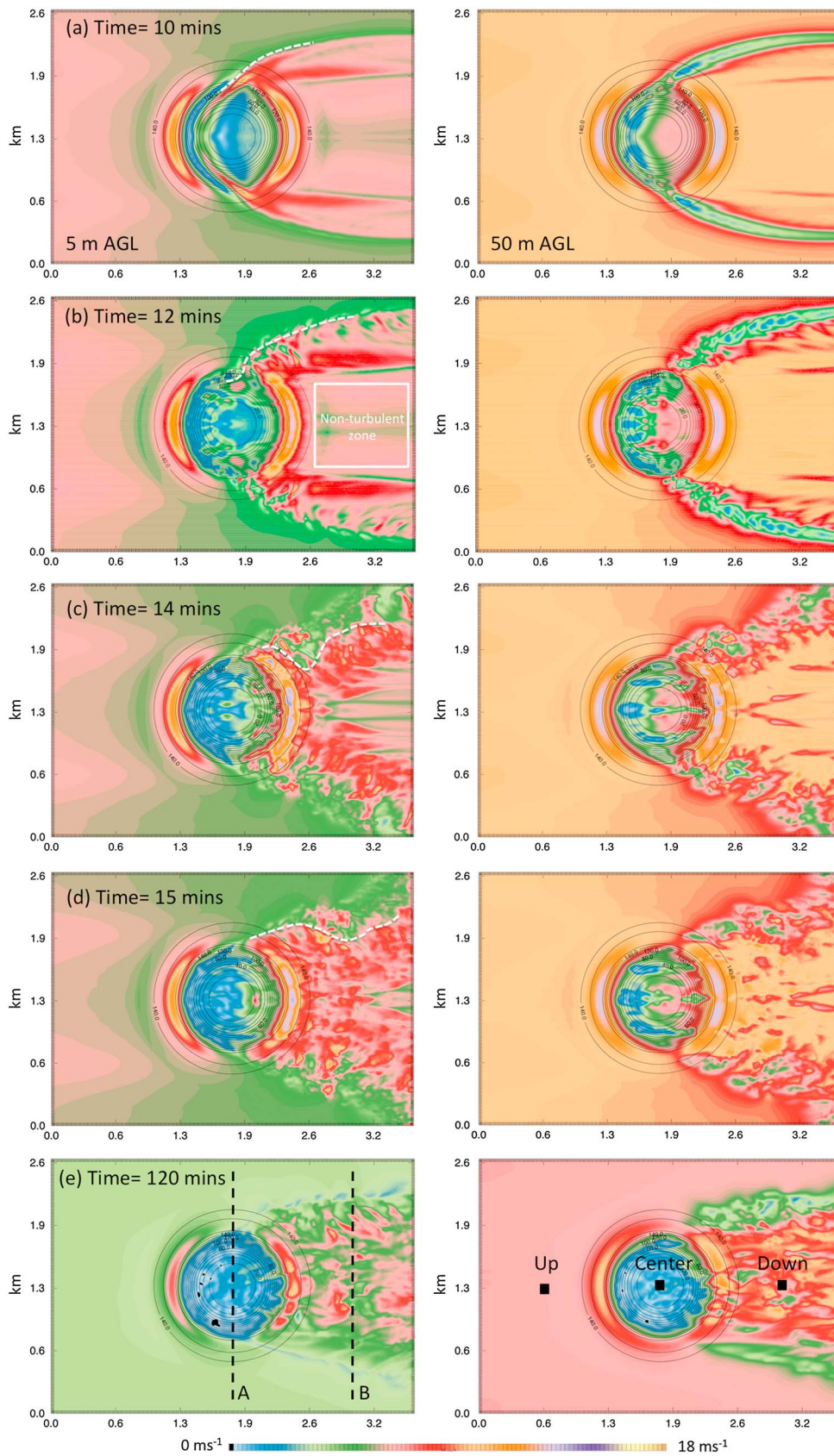
Figure 3. Horizontal cross section of wind speed (left) 5 and (right) 50 m AGL. (a-d) Snapshots from the first 15 min of the simulation are presented showing the evolution of the basin interior and wake turbulent boundary layer. White line outlines the evolution of the wake boundary into a fully developed one. (e) The quasi steady state after 2 h of running time.
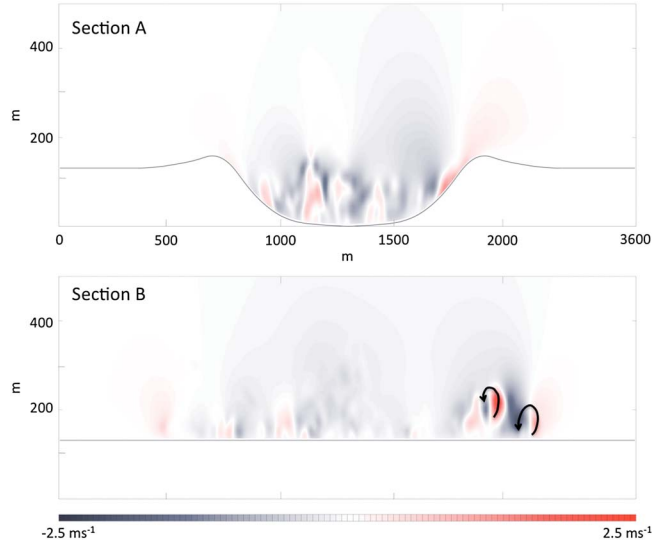
4

Figure 4. Vertical cross-flow sections of vertical velocity taken along lines A and B (Figure 3). The black arrows indicate rotational flow characteristic of wake eddies.

diffusion (M). The Coriolis parameter is omitted since the Coriolis force was neglected in the simulations due to the small spatial and temporal scales of the application.

[9] For turbulence, we focus our analysis on TKE, which may be written as in equation (2) (where m is the mass), along with its tendency in equation (3) (with coordinate system aligned with mean flow U for simplicity),

$$\frac{TKE}{m} = \bar{e} = 0.5\left(\overline{u'^2} + \overline{v'^2} + \overline{w'^2}\right) \tag{2}$$

$$\frac{\partial e^-}{\partial t} = A_e + S + D + M_e \tag{3}$$

where,

$$A_e = -\overline{U}\frac{\partial \overline{e}}{\partial x}$$

$$S = -\overline{u'w'}\frac{\partial \overline{U}}{\partial z}$$

$$D = -\varepsilon$$

$$M_e = -\frac{\partial}{\partial z}\left(\overline{w'e} + \frac{\overline{w'p'}}{\bar{\rho}}\right)$$

where e is the instantaneous TKE per unit mass ($m^2 s^{-2}$), U is wind ($m s^{-1}$), u', v', w' are velocity perturbations ($m s^{-1}$), t is the time coordinate (s), and ε is the eddy dissipation rate ($m^2 s^{-3}$), while overbars represent a time-averaged value. In this study, the buoyancy production/destruction term is omitted as the atmosphere is assigned with no vertical gradient in potential temperature (isentropic), while the subgrid-scale *TKE* advection (A_e) by the mean resolved wind, mechanical shear production and destruction (S), dissipation into friction heat (D), and turbulent mixing (M_e) that represents redistribution of TKE by pressure perturbations and turbulent eddies, all play a role in the subgrid-scale *TKE* conservation.

[10] All the wind speed, turbulence, and momentum profiles presented in the results section were temporally and spatially averaged. The simulations were run for 3 h until quasi-stationarity was achieved, and the averages were carried out on the final 1 h period. The velocity perturbations (as in equation (2)) used for the calculation of the resolved *TKE* were derived by subtracting the 15 min mean velocity from the total resolved velocity that was output by the model at 1 Hz frequency. The 15 min interval was chosen since this is a typical time period for the turnover of boundary layer eddies and because it falls within the range of the peak vertical velocity spectra from a similar wind speed magnitude and turbulence simulation of the same model used here. So the resolved *TKE* was calculated at every second along with the parameterized *TKE* and its budget terms, which were derived from the turbulence closure model used in the simulations. Resolved, parameterized, and total *TKE* budgets were then averaged spatially (over a 50 m by 50 m square area centered on the selected vertical profile locations as will be shown later) and temporally (over a 1 h period).

3. Results

[11] We begin by examining profiles of resolved and parameterized TKE. An inspection of the parameterized subgrid-scale *TKE* vertical profile output from the turbulence closure scheme reveals that the model is resolving more than 80% of the *TKE* and less than 20% is parameterized at the spatial resolution (10 m) used in the simulations (Figure 2). *Jiménez and Cuxart* [2005] tested the TKE1.5 closure scheme for LES at 5 m resolution and their percent contribution of SGS-TKE to the total TKE varied according to wind speed and stability within the range between 8.7 and 22%. Their results were from the vertically integrated SGS-TKE and resolved TKE and not a report of the maximum only as in our case (20%). If one were to vertically average the percent contribution of the subgrid-scale TKE in Figure 2, one would get a value anywhere between 10 and 15%. Furthermore, *Zhou and Chow* [2011] also investigated this particular aspect for the
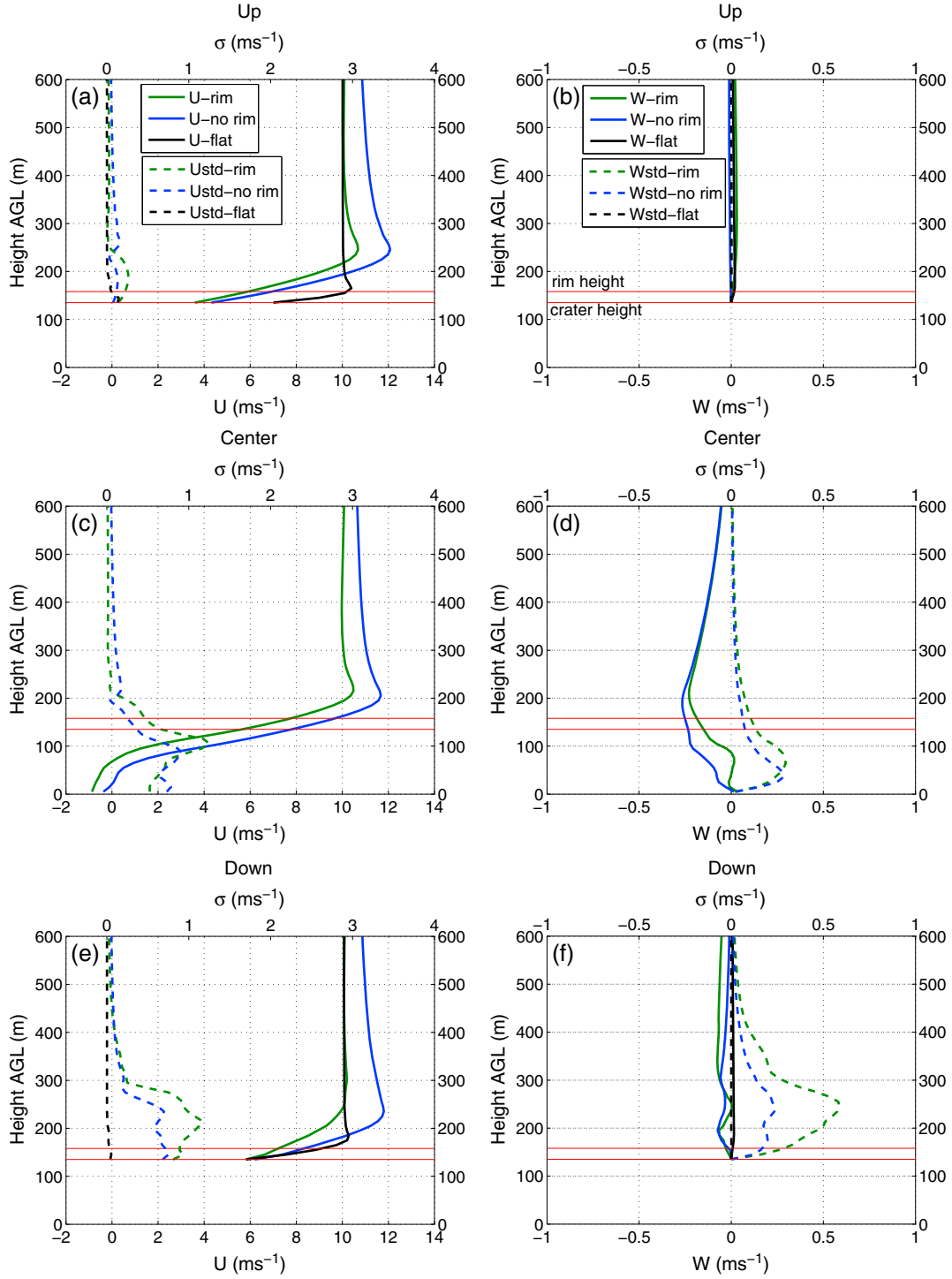
5

Figure 5. Vertical profiles of mean (solid lines) and standard deviation (dotted lines) of stream wise (U) and vertical (W) velocities. Profiles are constructed by averaging over a 5×5 grid point area (50 m × 50 m) around locations upstream (Up), central (Center), and downstream (Down) of the basin as shown in last panel of Figure 3. Green, blue, and black lines represent the *rim*, *no-rim*, and *flat* terrain cases. The red horizontal line indicates the height of the basin rim.

ARPS TKE-1.5 closure scheme, and their values were anywhere between 10 and 40% at the 5 m resolution. Hence, the ratio of parameterized to total TKE, associated with the spatial resolution used in this study, falls within the range of previously published results.

3.1. Turbulent Wake Evolution

[12] This section includes a description of the first 15 min of the simulation with specific focus on the turbulent boundary layer evolution within and in the wake of the basin. The process is described by showing horizontal cross sections
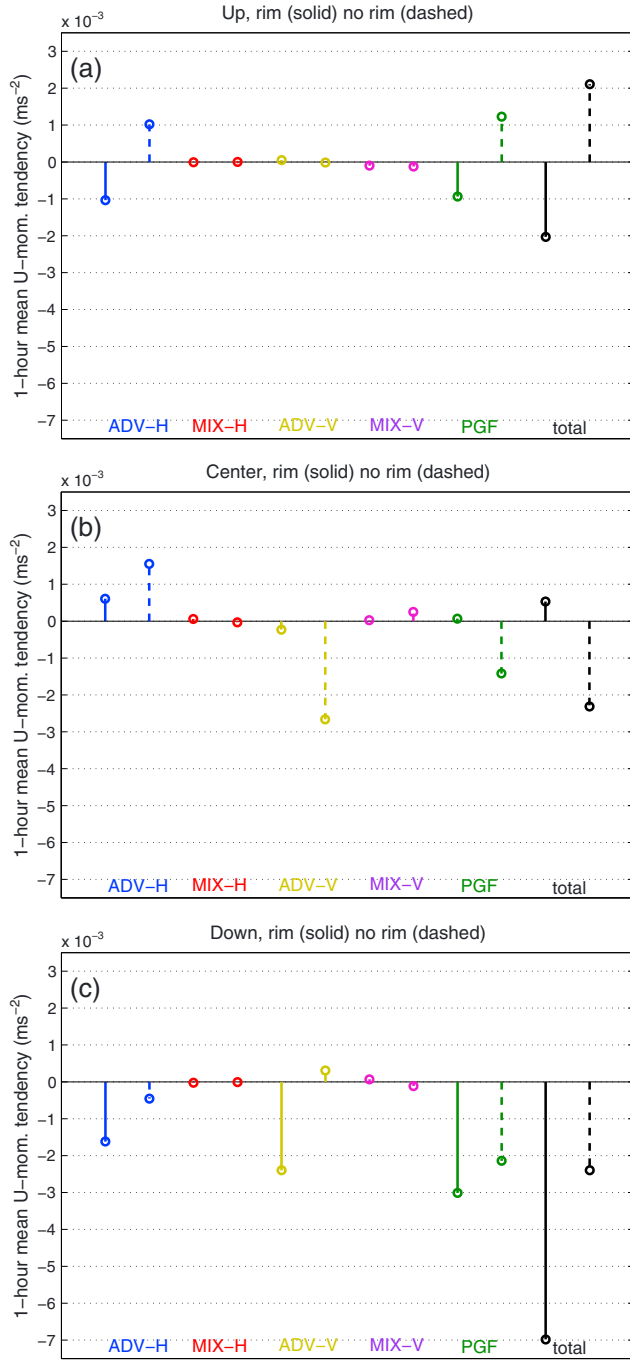
Figure 6. One hour average U-momentum tendency terms for locations upstream (Up), central (Center), and downstream (Down) of the basin for both the *rim* (solid lines) and *no-rim* (dashed lines cases). The Up and Down mean terms were extracted at 250 m AGL and spatially averaged over a 50 m by 50 m area; similarly, the Center location was extracted at 50 m AGL where the mean values have a maximum there. ADV, MIX, PGF, and total represent the momentum advection, mixing, pressure gradient forcing, and total tendency terms, while H and V are the horizontal and vertical directions, respectively.

of wind speed for the control simulation at 5 and 50 m above ground level (AGL) (Figure 3). After 10 min into the simulation, the basin terrain begins to produce perturbations in the near-surface flow fields as shown in Figure 3a. The basin interior experiences an overall reduction in wind speed mainly because of the piling up of air on the windward slope (the right-side slope facing the wind flow). This mass convergence produces a high-pressure perturbation that acts to oppose the flow and cause wind speed reduction inside the basin. As a consequence, the high pressure acts as a barrier to the main flow that deviates around it, goes up the north and south slopes and out of the crater. The high-pressure perturbation produces a discontinuity in wind speed (from low to high magnitudes) marked by a convergence zone on the northern slope of the basin (indicated by a dashed white line in Figure 3a). At times of 12, 14, and 15 min, the wake edge boundary (white dashed line) backs away from its original location (marked by the white dashed line in Figure 3a and then folds into the nonturbulent wake zone (marked by the white box), which then defines the turbulent wake of the basin. This wake edge represents a streamwise roll vortex that propagates in the direction of the flow and reveals an area of horizontal wind speed deficiency (green bands in Figure 3e) due to the vertical rotation shown in the vertical cross sections of vertical velocity in Figure 4. The wake and edge vortices can reach a height of 50 m above the surface.

[13] The upstream effect of the basin on the mean flow resembles the effect of a ship bow as it pierces through water. It is obvious throughout the first 15 min of the simulation how the effect of the basin as a decelerator of the incoming flow is manifested, thus the creation of the wave like interference in the upstream area of the basin that spans from north to south across the domain. This upstream effect appears to fade away in the 50 m AGL cross section and also in the quasi steady state of the simulation shown 2 h after initialization in Figure 3e.

[14] The evolution of the basin interior boundary at the 5 and 50 m height levels differs in the way eddies are organized. Near the surface, there is no clear organized structure with relatively homogeneous structural distribution and apparent spots of very weak wind speed (white and black areas in Figure 3e). At 50 m above basin floor, eddies in the center are organized parallel to the mean flow. These differences disappear after the boundary layers at those two different heights are well mixed and a quasi steady state is reached (Figure 3e). After 2 h into the simulation, the turbulent boundary layer of the basin with the rim, as shown in Figure 3e, has a clear distinct wake boundary restricted in width by the basin top diameter, an area of wind speed acceleration on top of the basin rim, and a relatively low wind speed interior with an occasional appearance of zero wind speeds in the convergence zones.

3.2. Mean Wind Speed and Momentum Budgets

[15] In this section, vertical profiles of mean horizontal and vertical wind speed are discussed in relation to the effect of the basin's rim from positions upstream (Up), central (Center), and downstream (Down) of the basin. Figure 5 shows the 1 h average and standard deviations of results from the *rim*, *no-rim*, and *flat* terrain simulations. Upstream from the basin, turbulence as measured by the standard deviations
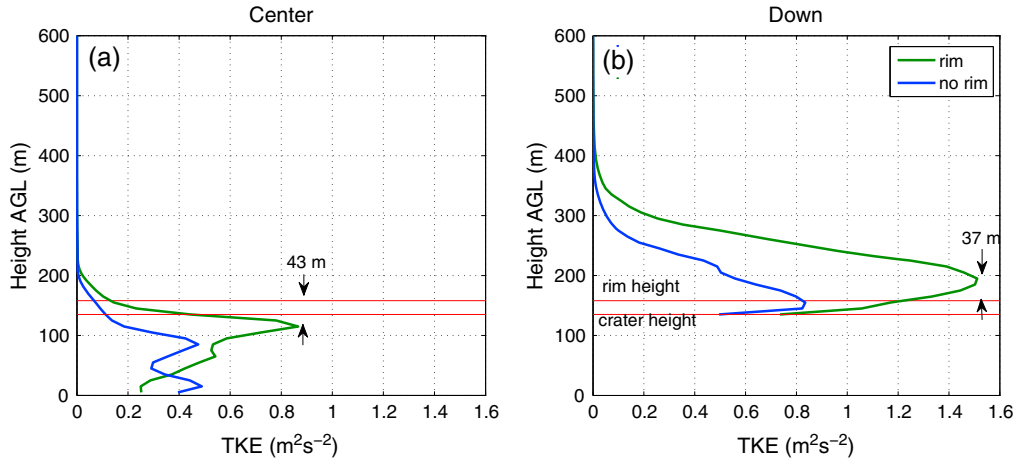
Figure 7. One hour average vertical profile of total TKE from basin center and downstream locations for both the *rim* and *no-rim* case.

of U and W velocities was minimal (Figure 5a), because the inflow and initial conditions did not include any turbulent perturbations. This experimental design allows for an investigation into the effects of terrain-induced turbulence only.

Comparison of the blue and green lines in Figure 5 shows the effect of the rim on the mean velocity. The *U*-velocity for all locations (Up, Center, and Down) decreases in magnitude when the rim is introduced. This decrease occurs at the
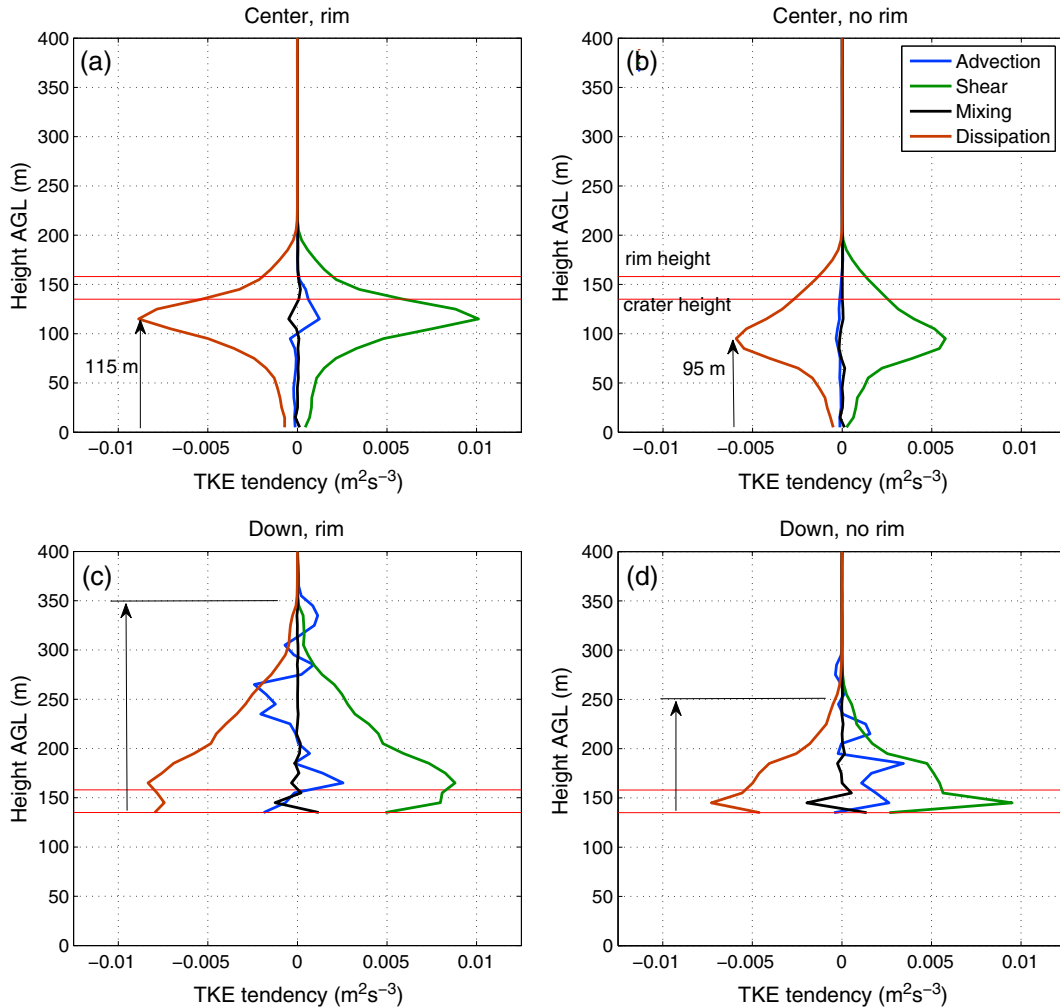
Figure 8. One hour average vertical profile of *TKE* time tendencies for basin center and downstream location from simulations (a and c) with and (b and d) without the rim.

expense of an increase in the standard deviation of the *U*-velocity for the rim case (green dashed lines). The total *U*-momentum forcing that the rim induces on the upstream flow, which is the sum of momentum advection, mixing, and the pressure gradient forcing, is negative for the *rim* case, as shown by the black lines in Figure 6a; this is in contrast to the *no-rim* case. These lines represent the 1 h average of total *U*-momentum tendency derived from the budget terms of the 1 h time series output at 1 min interval and extracted from a spatially averaged area (50 m by 50 m) at 250 m AGL. The difference in forcing between the *rim* and *no-rim* cases is mainly due to the contribution of the counter flow pressure gradient forcing (green line in Figure 6a) and horizontal advection of *U*-momentum induced by the rim upwind of the basin. Note that the contribution of momentum mixing forcing was minimal compared to the advective and pressure gradient forcing.

[16] The most significant change produced by the rim appears to be in the center and downstream regions where the standard deviations of both the *U* and *W*-velocity appear to be larger for the rim case. The other noticeable effect of the rim on the *U* and *W*-velocity is reflected in the first 75 m AGL in the basin center profiles (Figures 5c and 5d). The rim induces weaker vertical velocities and stronger return flows (negative *U*-velocity) with smaller horizontal standard deviations compared to the *no-rim* case. The return flow is restricted to the first 75 m above the surface of the basin center. The momentum budget analysis from a point 50 m above the basin floor (Figure 6b) suggests a less active environment for the *rim* case compared to the *no-rim* case. All three components of horizontal and vertical advection of *U*-momentum and the pressure gradient forcing are stronger for the *no-rim* case. The rim appears to limit momentum transfer inside the basin in the first 75 m above the basin floor because of blocking effects.

[17] Downstream of the basin, the vertical profiles of *U*-velocity resemble the profiles from a typical turbulent boundary layer, including a sheared profile near the surface and a smooth outer-layer homogeneous profile. Horizontal and vertical velocity perturbations measured by the *U* and *W*-velocity standard deviations for the *rim* case are still nearly double those in the *no-rim* case (green and blue dashed lines in Figured 5e and 5f). As opposed to the situation described above for the basin's interior environment and the blocking effect of the rim, the rim appears to induce more momentum transfer downstream than the *no-rim* case. The total *U*-momentum tendency (black line in Figure 6c) for the *rim* case is more negative than the *no-rim* case with more contribution from negative horizontal and vertical advection forcing compared to the *no-rim* case. The rate of change of the total *U*-momentum tendency from the downstream location only (not shown here) shows a nearly two-fold increase for the *rim* case as opposed to a sixfold increase for the *no-rim* case. This suggests that the rim was acting effectively as a physical obstruction to the flow at the simulated model resolution.

3.3. TKE

[18] By deriving the total *TKE*, as outlined in section 2, one can compare the vertical distribution of turbulence from locations at the center and downstream of the basin with and without the rim (Figure 7). The *TKE* for the *no-rim* case

downstream of the basin (blue line in Figure 7b) shows a typical profile over flat terrain with a maximum near the surface and a decreasing profile aloft. The introduction of the rim induces two changes: an approximate doubling of the amount of *TKE* and a vertical height offset of the peak by an amount that scales to the rim height (~37 m). The *TKE* profile inside the basin is shown in Figure 7a. The *no-rim* case (blue line) shows a vertically homogeneous *TKE* profile with values around 0.4 $m^2 s^{-2}$ up to 100 m AGL, with decreasing *TKE* above. The introduction of the rim (green line) produces a less homogenous vertical distribution of *TKE* with an increase from the surface up to a peak (0.8 $m^2 s^{-2}$) at the 43 m level that is nearly double the magnitude of the *no-rim* case. (Figure 7a).

[19] The vertical profiles of *TKE* tendency presented in Figure 8 divide the subgrid-scale *TKE* tendency into its budget terms of advection, shear production, turbulent mixing, and dissipation. The plots reveal which terms of the *TKE* budget equation (equation (2)) dominate when the effect of the rim is introduced. The effect of the rim on various *TKE* budget terms is mainly reflected in higher magnitudes in the upper levels of the basin (>75 m for Figures 8a and 8b). Similarly, downstream from the basin (Figures 8c and 8d), the introduction of the rim produces higher magnitudes of *TKE* budget terms for areas up to 350 m AGL (100 m higher than the *no-rim* case, compare arrows for Figures 8c and 8d). Inside the basin, most of the *TKE* in the *rim* case comes from shear production, and consequently *TKE* dissipation follows the profile of the shear production. Also, the rim feature yields a layer of positive *TKE* advection (blue line in Figure 8a), which does not exist in the *no-rim* case (Figure 8c). Downstream of the basin, apart from the near-surface *TKE* mixing (black line in Figures 8c and 8d), *TKE* advection and shear production dominate the total *TKE* budget for both the *rim* and *no-rim* cases. For the *no-rim* case (Figure 8d), the effect of the basin on downstream *TKE* is evident up to around 100 m AGL with a positive advection of *TKE*. The presence of the rim induces positive low-level *TKE* advection, and negative high-level *TKE* advection up to 200 m above the surface, and more *TKE* shear production and dissipation. The oscillation in the *rim* case *TKE* advection profile appears to be the result of the larger-scale eddies produced by the rim promoting mixing of high-level weak turbulence with low-level strong turbulence, which is then advected by the mean horizontal velocity.

4. Discussion

[20] The ARPS model, at the selected 10 m spatial resolution, was able to resolve between 80 and 90% of the total *TKE* field. As is the case with most LES models, the turbulence field was less resolved and more parameterized near the wall boundaries, but still within the 80–90% range.

[21] The first 15 min of the simulations illustrated the evolution of the turbulent boundary layer within and in the wake of the basin. Results showed that the slopes of the crater play an important role in defining and later creating the turbulent boundary wake. Roll vortices initiate at the upper and lower slopes crosswise to the main flow direction, and then propagate up, outward, and eventually fold in to form what will later become the turbulent wake boundary layer. Given the symmetric nature of the basin, the initial separation
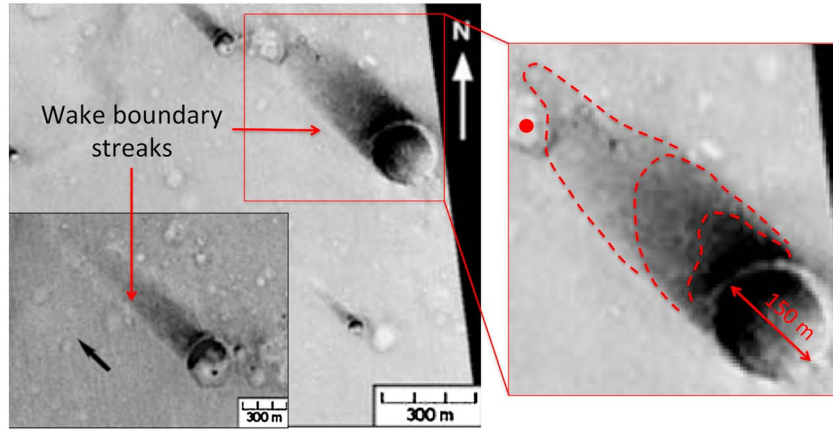
Figure 9. The floor of Gusav Crater, Mars, presented in a satellite-derived thermal infrared image adapted from *Greeley et al.* [2003]. Areas of high albedo (light streaks) and areas of low albedo (dark areas in crater's wake) show effects of strong winds in erosion and modification of surface type from fine particles (high albedo) to the exposition of larger-sized sand grains (low albedo). The image also shows an increasing albedo gradient outlined by the red dashed lines indicating areas of high wind speeds initially in the immediate wake of the crater and reduction of wind speed more downstream of the crater. Black arrow indicates wind direction.

induced by the slope roll vortices happens approximately in the center, but with the same physical reasoning, one would expect the shift of this initial separation zone farther upstream if the slope angle in the downwind side of the basin was increased. This process was short lived, lasting only for around 15 min, but would otherwise repeat itself in scenarios where intermittent winds are prevailing over the basin or similar topography, which suggests that in intermittent wind regimes most of the scalar transport from near the basin slope happens through the described dynamics.

[22] Careful examination of thermal infrared images of the Martian surface [*Greeley et al.*, 2003] (Figure 9) shows resemblance to the wake flow field simulated in this study. In Figure 9, the dark and light colors represent areas of low and high albedo, respectively. Low albedo (dark color) results from the wind displacement of fine particles that leave an area of relatively coarser sand grain size, which absorbs more shortwave radiation; hence, dark colors in Figure 9 represent stronger wind speeds. Conversely, high albedo (light color) results from the settling or transfer of finer sand particles, which represents areas of relatively low wind speeds. The wind erosion footprints presented in Figure 9 represent the strongest wind speed regime and dominant wind direction the crater experiences. Features of interest are the light streaks (indicated by the red arrows), which appear to be common features for various crater images and allude to the fact that these regions may have lower wind speeds than their surroundings, and hence favor the distribution of fine sand grain size (high albedo). Resemblance to the wake boundary edges of our simulations in Figure 3e (blue shades) is evident.

[23] The 30 m high rim is found to have an effect on the mean wind speeds at least 600 m upstream from the basin. The major effect is reflected as a 10% reduction in wind speed at 120 m AGL. Although such a change in wind speed may appear small, it can be significant for applications such as wind turbine siting where the power extracted from the wind is a function of the third power of the wind speed.

Our momentum budget analysis suggests two possible mechanisms contributing to flow deceleration upstream of the crater when the rim is introduced: the first is the pressure gradient force that is negative in sign compared to the no-rim case (Figure 6a), and the second is the negative advection of horizontal momentum. It is also possible that some aspects of flow deceleration may be attributed to the indirect effect of the rim on the turbulent layer produced above the crater, which in turn feeds back on the laminar boundary layer of the inflow conditions. Due to the lack of atmospheric stability, it is accurate to say that the flow deceleration is not due to blocking as a result of Froude number principle (a principle that relates upstream atmospheric stability and topography dimensions to flow modifications), but merely to subtle interactions of the laminar (inflow) and turbulent crater boundary layer, which are reflected in the obtained momentum budgets.

[24] These findings suggest that even in areas of relatively flat terrain, such as the Great Plains of the United States, the effects of small terrain features should be considered for wind turbine siting. Another feature of interest from the Martian surface (Figure 9) that might present at least qualitative validation to the above mentioned point is the asymmetric distribution of the crater's wake (see red bounded box in Figure 9). The downwind terrain feature (indicated by the red dot) appears to be responsible for this asymmetry, especially when comparing the wake to other crater wakes in the region that lack any downwind obstacle. The upstream modification manifests as a reduction in upstream wind speeds (marked by the less erosion upwind of the red dot), which can be explained by the counterflow pressure gradient forcing imposed by the obstacle, similar to the explanation provided for the upwind effect of the rim in our simulations.

[25] Inside the basin, the presence of a rim produces more recirculation from the basin floor to 75 m above as measured by the U-velocity. However, the vertical velocity over the same height range is near zero suggesting that lateral circulation within the basin interior dominates over vertical circulation. The rim acts to limit momentum transfer in the lower

half of the basin, which suggests a mechanical forcing effect (or topographic blocking) induced by the rim on the lower basin environment. This would act as an extra forcing in creating a quiescent basin interior environment decoupled from the exterior one.

[26] Downstream of the basin center, the rim produced a reduction in wind speed magnitude at least 600 m downstream from the basin where the profile analysis was taken from. This reduction in wind speed was primarily a consequence of more turbulent eddies shed by the rim and their influence on the momentum budget downstream of the basin. The rim induced more negative momentum tendencies primarily through negative advection and pressure gradient forces, which resulted in the deceleration of the flow downstream of the basin.

[27] In the *rim* simulation, the TKE maximum is located about 43 m below the rim height, whereas in the *no-rim* simulation, overall TKE magnitudes are smaller, and there is a secondary peak near the surface. This location of high TKE (in the *rim* simulation 43 m below the rim) scales to the rim height itself (30 m), and rim-induced TKE magnitudes were twice as large as in the *no-rim* case. This increase in TKE was primarily a result of TKE advection of rim-induced turbulence. This critical height level (43 m below the rim height) acts as the most favored location for TKE production and destruction, hence its potential importance for the top-to-bottom turbulence erosion of basin boundary layers. At the surface, the impact of the rim on the TKE is reversed compared to the upper level of the basin, and the rim appears to minimize the TKE compared to the *no-rim* case. A possible physical explanation for this may be that the rim is acting to reduce the lee turbulence produced by the basin slope by effectively increasing the length or height of the slope, which would then change the size and spatial distribution of the leeside wake inside the basin.

[28] Downstream of the basin, the *TKE* vertical profile resembles those over flat terrain, with a peak very close to the surface and a decrease in magnitude with height. The rim-induced change in the downstream *TKE* appears as a vertical shift in the peak of *TKE* by an amount (37 m) that scales to the rim height (30 m), due likely to the shedding of eddies from the rim that induces the velocity perturbation downstream of their source.

5. Conclusion

[29] LESs of turbulent flows inside and downstream of a small circular basin were performed using the ARPS model. The analysis of the simulation results focused on the terrain-induced turbulence inside and in the wake of the basin and on the effect of the introduction of a 30 m high rim around the basin top. Numerical simulations of cases with/without the small basin and with a basin but with/without the rim highlight the important effects of small terrain features on both the mean and turbulent flows. The results from this research indicate that small terrain features in the proximity of larger ones can induce relatively large modifications to the mean and turbulent flows. These modifications need to be considered when interpreting observational data or results from numerical simulations that do not resolve such features. More importantly, the model results show that TKE doubles inside the crater due to the effect of the rim, which follows the observed trend under similar but not identical ambient conditions in *Fu et al.* [2010]. The most critical point for the reader to take away from this paper is that the impact of small terrain features (e.g., the rim surrounding Meteor Crater) on mean and turbulent flow is not necessarily restricted to the local environment. Thus, we advise caution when interpreting observations or modeling results where such features are unresolved.

[30] Although the analysis in the study was restricted to neutral atmospheric profiles, and large-scale turbulent perturbations were excluded, we intend to expand the work and incorporate modifications from thermally driven turbulence and its interaction with small terrain features in future work. Every scientific investigation is bound with the assumptions made in the beginning and also bound to the scale under investigation. This study only focused on terrain-induced turbulence with no large-scale background turbulence, so there is a possible overestimation of the terrain effect as a result of our simplified experiment design.

References

Beare, R. J., et al. (2006), An intercomparison of large-eddy simulations of the stable boundary layer, *Boundary Layer Meteorol.*, *118*, 247–272.

Bougeault, P., P. Binder, A. Buzzi, R. Dirks, R. Houze, J. Kuettner, R. B. Smith, R. Steinacker, H. Volkert (2001), The MAP special observing period, *Bull. Am. Meteorol. Soc.*, *82*, 433–462.

Chow, F. K., A. P. Weigel, R. L. Street, M. W. Rotach, and M. Xue (2006), High-resolution large-eddy simulations of flow in a steep alpine valley. Part I: Methodology, verification, and sensitivity experiments, *J. Appl. Meteorol. Clim.*, *45*, 63–86.

Colette, A., F. K. Chow, and R. L. Street (2003), A numerical study of inversion-layer breakup and the effects of topographic shading in idealized valleys, *J. Appl. Meteorol.*, *42*, 1255–1272.

Deardorff, J. W. (1980), Stratocumulus-capped mixed layers derived from a 3-dimensional model, *Boundary Layer Meteorol.*, *18*, 495–527.

Doyle, J. D., V. Grubisic, W. O. J. Brown, S. F. J. De Wekker, A. Dornbrack, Q. F. Jiang, S. D. Mayor, and M. Weissmann (2009), Observations and numerical simulations of subrotor vortices during T-REX, *J. Atmos. Sci.*, *66*, 1229–1249.

Dupont, S., Y. Brunet, and J. J. Finnigan (2008), Large-eddy simulation of turbulent flow over a forested hill: Validation and coherent structure identification, *Q. J. R. Meteorol. Soc.*, *134*, 1911–1929.

Fedorovich, E., R. Conzemius, I. Esau, F. Chow, D. Lewellen, C. H. Moeng, P. Sullivan, D. Pino, and J. V. G. de Arellano (2004), Entrainment into sheared convective boundary layers as predicted by different large eddy simulation codes, preprints in the 16th Symposium on Boundary Layers and Turbulence, Am. Meteorol. Soc., 9–13.

Fesquet, C., S. Dupont, P. Drobinski, T. Dubos, and C. Barthlott (2009), Impact of terrain heterogeneity on coherent structure properties: Numerical approach, *Boundary Layer Meteorol.*, *133*, 71–92.

Fritts, D. C., D. Goldstein, and T. Lund (2010), High-resolution numerical studies of stable boundary layer flows in a closed basin: Evolution of steady and oscillatory flows in an axisymmetric Arizona Meteor Crater, *J. Geophys. Res.*, *115*, D18109, doi:10.1029/2009JD013359.

Fu, P., S. Zhong, C. D. Whiteman, T. Horst, and X. Bian (2010), An observational study of turbulence inside a closed basin, *J. Geophys. Res.*, *115*, D23106, doi:10.1029/2010JD014345.

Greeley, R., R. O. Kuzmin, S. C. R. Rafkin, T. I. Michaels, and R. Haberle (2003), Wind-related features in Gusev crater, Mars, *J. Geophys. Res.*, *108*(E12), 8077, doi:10.1029/2002JE002006.

Greeley, R., et al. (2008), Columbia Hills, Mars: Aeolian features seen from the ground and orbit, *J. Geophys. Res.*, *113*, E06S06, doi:10.1029/2007JE002971.

Jiménez, M., and J. Cuxart (2005), Large-eddy simulations of the stable boundary layer using the standard Kolmogorov theory: Range of applicability, *Boundary Layer*, *115*, 241–261.

Katurji, M., and S. Zhong (2012), The influence of topography and ambient stability on the characteristics of cold-air pools: A numerical investigation, *J. Appl. Meteorol. Climatol.*, *51*, 1740–1749, doi:10.1175/JAMC-D-11-0169.1.

Katurji, M., A. Sturman, and P. Zawar-Reza (2011a), An investigation into ridge-top turbulence characteristics during neutral and weakly stable conditions: Velocity spectra and isotropy, *Boundary Layer Meteorol.*, *139*, 143–160.

Katurji, M., S. Zhong, and P. Zawar-Reza (2011b), Long-range transport of terrain-induced turbulence from high-resolution numerical simulations, *Atmos. Chem. Phys.*, *11*, 11,793–11,805.

Kiefer, M. T., and S. Zhong (2011), An idealized modeling study of nocturnal cooling processes inside a small enclosed basin, *J. Geophys. Res.*, *116*, D20127, doi:10.1029/2011JD016119.

Kirshbaum, D. J., and R. B. Smith (2009), Orographic precipitation in the tropics: Large-eddy simulations and theory, *J. Atmos. Sci.*, *66*, 2559–2578.

Klemp, J. B., and D. R. Durran (1983), An upper boundary condition permitting internal gravity wave radiation in numerical mesoscale models, *Mon. Weather Rev.*, *111*, 430–359.

Lehner, M., and C. D. Whiteman (2012), The thermally driven cross-basin circulation in idealized basins under varying wind conditions, *J. Appl. Meteorol. Climatol.*, *51*, 1026–1045.

Lilly, D. K. (1967), The representation of small-scale turbulence in numerical simulation experiments, paper presented at IBM Scientific Computing Symposium on Environmental Science, Yorktown Heights, N. Y.

Moraes, O., O. Acevedo, G. Degrazia, D. Anfossi, R. da Silva, and V. Anabor (2005), Surface layer turbulence parameters over a complex terrain, *Atmos. Environ.*, *39*, 3103–3112.

Rotach, M. W., and D. Zardi (2007), On the boundary layer structure over highly complex terrain: Key findings from MAP, *Q. J. R. Meteorol. Soc.*, *133*, 937–948.

Sagaut, P. (2001), *Large Eddy Simulations for Incompressible Flows: An Introduction*, 585 pp., Springer, Berlin.

Savage, L. C., S. Zhong, W. Yao, W. J. O. Brown, T. W. Horst, and C. D. Whiteman (2008), An observational and numerical study of a regional-scale downslope flow in northern Arizona, *J. Geophys. Res.*, *113*, D14114, doi:10.1029/2007JD009623.

Schär, C., and Smith R. B. (1993), Shallow-water flow past isolated topography. I: Vorticity production and wake formation, *J. Atmos. Sci.*, *50*, 1373–1400.

Smith, R. B., A. C. Gleason, P. A. Gluhosky, and V. Grubisic (1997), The wake of St. Vincent, *J. Atmos. Sci.*, *54*, 606–623.

Volkert, H., and T. Gutermann (2007), Inter-domain cooperation for mesoscale atmospheric laboratories: The meso-scale alpine programme as a rich study case, *Q. J. R. Meteorol. Soc.*, *133*, 949–967.

Weigel, A. P., F. K. Chow, M. W. Rotach, R. L. Street, and M. Xue (2006), High resolution large-eddy simulations of flow in a steep alpine valley, Part II: Flow structure and heat budgets, *J. Appl. Meteorol. Climatol.*, *45*, 87–107.

Whiteman, C. D., et al. (2008), METRCRAX 2006: Meteorological experiments in Arizona's meteor crater, *Bull. Am. Meteorol. Soc.*, *89*, 127–150.

Whiteman, C. D., S. W. Hoch, M. Lehner, and T. Haiden (2010), Nocturnal cold-air intrusions into a closed basin: Observational evidence and conceptual model, *J. Appl. Meteorol. Climatol.*, *49*, 1894–1905.

Xue, M., et al. (2001), The Advanced Regional Prediction System (ARPS) – A multi-scale nonhydrostatic atmospheric simulation and prediction tool. Part II: Model physics and applications, *Meteorol. Atmos. Phys.*, *76*, 143–165.

Zhou, B., and F. K. Chow (2011), Large-eddy simulation of the stable boundary layer with explicit filtering and reconstruction turbulence modeling, *J. Atmos. Sci.*, *68*, 2142–2155.